

# Probing Phase Diagrams of Ordered Two-Dimensional Ice

Bingzheng Wu<sup>1</sup>, Jianming Wu<sup>1</sup>, Sai Duan<sup>1,2\*</sup>, & Xin Xu<sup>1,2\*</sup>

<sup>1</sup>*State Key Laboratory of Porous Materials for Separation and Conversion, Shanghai Key Laboratory of Molecular Catalysis and Innovative Materials, MOE Key Laboratory of Computational Physical Sciences, Research Center for Chemical Theory, Department of Chemistry, Fudan University, Shanghai 200438, P. R. China*

<sup>2</sup>*Hefei National Laboratory, Hefei 230088, P. R. China*

**Water, a ubiquitous and fundamental substance, plays a critical role across a wide range of disciplines from physics and chemistry to biology and engineering. Despite theoretical predictions of several phases of two-dimensional (2D) ice confined between idealized hydrophobic walls, experimental validation has been limited to the square phase, whose structural origin remains controversial. Here, we propose a realistic nanoconfinement setup using wide-bandgap hexagonal boron nitride (h-BN) as the capping layer and Cu(111) as the substrate. This protocol enables scanning tunneling microscope (STM) to resolve the atomic-scale arrangement of water molecules beneath the h-BN layer, overcoming the limitations of conventional techniques. Simulated STM images unambiguously identify all ordered flat 2D ice phases, as well as coexisting phases, and effectively distinguish them from potential contaminants. These findings establish a robust framework for experiment to systematically probe the phase structures of 2D ice, opening an avenue for studying nanoconfined water under ambient conditions.**

Water is the most essential chemical substance for life on our planet<sup>1,2</sup>. One of the remarkable characteristics of bulk water is its array of anomalous physical properties<sup>3,4</sup>, which are intrinsically linked to its diverse phase structures<sup>5,6</sup>. Consequently, exploration of the water's phase diagrams has been a central theme for over a century<sup>7-9</sup>. When water is confined to lower dimensions, conditions prevalent in interfacial systems, its behavior becomes even more intriguing. For instance, water molecules confined in nanoslits exhibit a range of unusual physicochemical properties, such as peculiar ion permeability<sup>10</sup>, anomalous low dielectric constant<sup>11</sup> and friction coefficient<sup>12</sup>, as well as significantly enhanced shear viscosity<sup>13</sup> and thermal conductivity<sup>14</sup>. As in the bulk, efforts have been made to correlate these anomalous behaviors with structural features through proposed hypotheses<sup>10,11,15</sup> and theoretical models<sup>16</sup>. However, in low-dimensional systems, definitive structure-property relationships, comparable to those established for three-dimensional water, remain elusive.

This challenge primarily stems from the lack of chemically resolved atomic-scale characterization techniques to determine the phase structures of confined water. Although several structures without confinement, such as buckled pentagonal rings coexisting with heptagonal<sup>17</sup> and hexagonal arrangements<sup>18</sup>, have been observed, fully studying the phase diagrams of two-dimensional (2D) ice requires confinement to generate the necessary pressure, which inevitably imposes limitations on the applicability of conventional measurement techniques<sup>19-23</sup>. As a result, compared to bulk, experimental approaches on structural characterization of nanoconfined 2D ice remain scarce.

Algara-Siller et al. pioneered the experimental investigation of 2D ice under lateral pres-

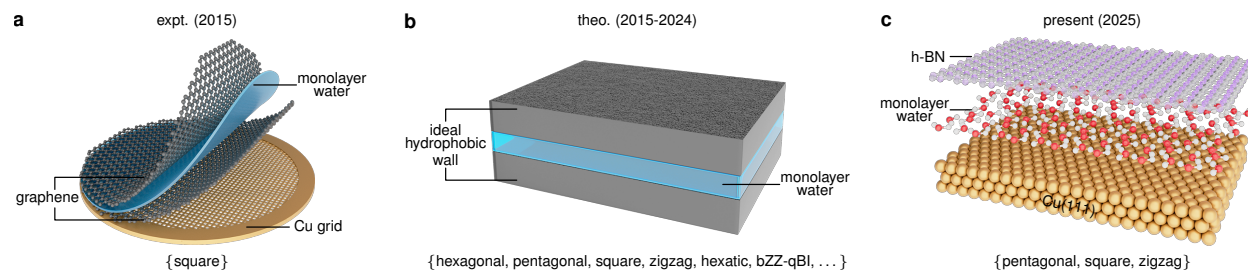


**Figure 1: Configurations for 2D ice phases.** **a**, A water monolayer confined between two graphene monolayers, with the bottom sheet supported on a Cu grid. With this setup, experimental measurements via transmission electron microscopy (TEM) speculated a square arrangement of the water molecules. **b**, Hydrophobic walls were used in theoretical simulations to explore phase diagrams of nanoconfined 2D ice. This idealized configuration approximates the van der Waals interactions between nanoslits and water molecules but does not correspond to a realistic experimental setup. **c**, The setup proposed in this work, where a water monolayer is confined between a realistic Cu(111) substrate and a scanning tunneling microscope (STM)-transparent h-BN capping layer. The publication years of the respective studies are labeled in parentheses, and the proposed or observed phases are labeled in the braces.

sure by confining water between two graphene sheets (Figure 1a)<sup>24</sup>. Using transmission electron microscopy (TEM)<sup>24</sup>, they observed an ordered “square” ice structure at a lateral pressure of approximately 1 GPa, opening the door for the study of nanoconfined ice. Subsequent theoretical studies, which employed idealized hydrophobic walls as the confinement layers (Figure 1b), revealed a rich phase diagram of 2D water. Specifically, Chen et al. successfully reproduced the experimentally observed “square” structure and identified additional arrangements, such as pentagonal and buckled rhombic arrangements under varying lateral pressures and confinement widths

at 0 K<sup>25</sup>. By further considering temperature effects, theoretical phase diagrams of 2D ice were subsequently proposed<sup>26–29</sup>, indicating that these ordered structures remain stable over a wide range of temperatures from 0 to 170 K.

Despite a variety of 2D ice structures predicted by theory, direct comparison between theoretical models and experimental observations remains challenging due to the exclusive use of idealized hydrophobic confinement potentials and a primary reliance on energetic calculations<sup>25–29</sup>. In fact, to date, the only experimentally observed arrangement remains the initially reported square structure<sup>24</sup>. However, the precise identification of this structure is still under debate because of the lack of chemical resolution of TEM imaging. Zhou et al. argued that sodium chloride (NaCl), a common contaminant in graphene, cannot be excluded, as it exhibits a similar structure and lattice constant that cannot be distinguished from the 2D square ice by TEM<sup>30</sup>. Therefore, to eliminate plausible candidates with similar geometrical parameters and thus to establish definitive evidence for the structures of nanoconfined 2D ice, a characterization technique that combines both spatial and chemical resolution is urgently needed.

In this work, we propose a setup that enables the leverage of the chemical sensitivity of scanning tunneling microscope (STM) to characterize different phase structures of 2D ice (Figure 1c). In this protocol, the Cu(111) surface is selected as the substrate because of its inherent hydrophobicity and high electrical conductivity<sup>31</sup>. Meanwhile, hexagonal boron nitride (h-BN) is chosen as the capping layer, which provides the required lateral pressure for stabilizing various 2D ice phases while remaining STM-transparent owing to its 2D structure and wide bandgap<sup>32–34</sup>. By

adjusting the confinement width between h-BN and Cu(111), lateral pressures applied to 2D ice can be effectively controlled<sup>25</sup>. Simulations based on this setup<sup>31,35–38</sup> demonstrate that STM measurements can clearly distinguish not only between different ordered ice phases but also between these phases and potential contaminants such as NaCl. Hence, this approach provides a unique and robust platform that all ordered phase structures of 2D ice can be unambiguously identified and explored, for the first time.

## Results and discussion

### \* Identifying the square phase of 2D ice

We begin by examining the only experimentally observed ordered arrangement, namely the “square” structure<sup>24</sup>. The optimized geometry of this square 2D ice, confined between h-BN and Cu(111) at a confinement of 5.7 Å, is depicted in Figure 2a. The primary structural feature of this 2D ice, i.e., square units formed by four oxygen atoms at the vertices, agrees well with previous experimental<sup>24</sup> and theoretical results<sup>25,26</sup>, despite that the latter adopted idealized hydrophobic repulsive wall potentials. Notably, due to the presence of the realistic Cu(111) substrate and h-BN capping layer, a slight structural distortion is observed with some O–H bonds pointing towards the metallic substrate. The calculated lateral pressure is 0.9 GPa, well within the previously reported range of 0.6–1.7 GPa from simulations<sup>26</sup>. Therefore, the minor structural deviations induced by inevitably water-substrate interactions in realistic conditions do not preclude the identification of this configuration as the square 2D ice phase.

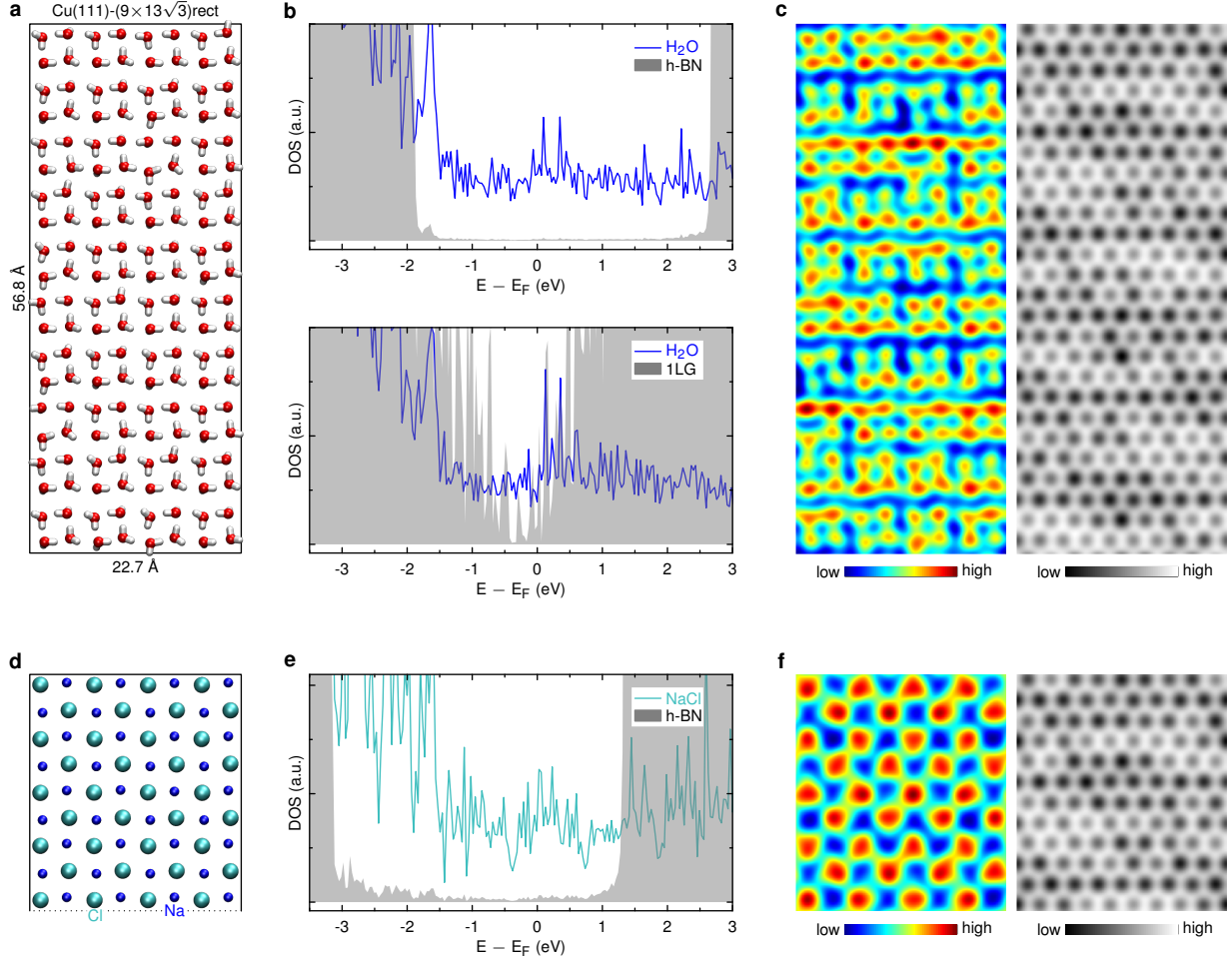


Figure 2: **Identification of the square 2D ice.** **a**, Top view of the optimized geometry of the square 2D ice confined between a h-BN layer and a Cu(111) surface, with a confinement width of 5.7 Å. The lattice constants (in Å) of the heterogeneous layers and the supercell of Cu(111) are labeled. **b**, Projected density of state (DOS) for the square 2D ice system with a single h-BN layer (top) and a single graphene layer (1LG, bottom) as the capping layer. **c**, Simulated STM images for confined square 2D ice with h-BN (left) and graphene (right) as the capping layer. **d**, Top view after replacing the water layer in panel (a) with a NaCl layer. **e**, Projected DOS for the system of NaCl capped by h-BN. **f**, Simulated STM images of confined NaCl with a single h-BN layer (left) and a single graphene (right) as the capping layer. All STM simulations were performed at a sample bias of  $-0.5$  V.

The calculated density of states (DOS) reveals that the contribution from the top h-BN layer near the Fermi level is negligible (Figure 2b, top panel), attributable to its wide bandgap of around 4 eV<sup>32-34</sup>. In contrast, the DOS contribution from the water layer is two orders of magnitude higher than that of h-BN, indicating that the underlying 2D ice structures can be readily detected by STM. Indeed, the simulated STM image shows distinct protrusions corresponding to oxygen atoms beneath the h-BN layer (Figure 2c, left panel), confirming that the STM transparency of h-BN enables chemically resolved imaging of the 2D ice. It is noted that the STM pattern is slightly non-uniform with fused oxygen atoms in some rows. This heterogeneity reflects the influence of lattice mismatch between the 2D ice and the metallic substrate.

To highlight the STM transparency of h-BN, we further simulated the same confined “square” ice structure between a graphene layer and Cu(111), a configuration that closely resembles the experimental setup used in TEM study<sup>24</sup>. Due to the unique band structure of the Dirac cone<sup>39,40</sup>, the DOS near the Fermi level is dominated by the graphene layer, despite a slight increase in the DOS contribution from the water molecules (Figure 2b, bottom panel). As a result, STM measurements cannot effectively probe through the graphene capping layer and are thus unable to resolve the structural arrangement of the underlying 2D ice. Instead, only the characteristic honeycomb pattern of graphene is observed in the simulated STM image (Figure 2c, right panel). This contrast underscores the critical importance of using wide bandgap h-BN as the capping layer to enable STM transparent confinement, thereby allowing chemically resolved imaging of the structures beneath the capping layer, which is inaccessible in other scanning probe techniques<sup>41-45</sup>.

Another key advantage of the current setup is its capability to identify the debated contaminants<sup>24,30</sup>. To this end, we replaced the water molecules in the square 2D ice with sodium and chlorine atoms in a 1:1 stoichiometric ratio, simulating a potential NaCl contaminant<sup>30</sup> that may be introduced during the transfer of 2D materials or from environmental pollutions (Figure 2d). In this scenario, the bandgap of h-BN remains intact but exhibits a significant negative band offset (Figure 2e). Accordingly, h-BN again exhibits negligible DOS near the Fermi level. Meanwhile, the DOS of the NaCl layer is comparable to that of the square 2D ice. Consequently, the structure of the confined NaCl is also detectable via STM. Interestingly, due to the dominant contribution of the Cl atoms (Extended Data Figure 1), the corresponding STM image has a significantly (around 1.4 times) larger lattice of the square unit cell with a 45° rotation compared to that of the 2D ice (Figure 2f, left panel). These distinct structural and electronic signatures enable unambiguous differentiation between square 2D ice and NaCl, helping to resolve a long-term controversy in this subject. Again, when graphene is used as the capping layer, the Dirac cone (Supplementary Figure 1) causes the honeycomb pattern to dominate the corresponding STM image, masking any signal from the beneath NaCl layer (Figure 2f, right panel).

Notably, the square arrangement of 2D ice is robust. For instance, when the primitive water unit cell reported in Ref. 27 is used, the aspect ratio of the supercell is significantly decreased. Nevertheless, the confinement width is only slightly reduced from 5.7 to 5.5 Å to maintain the required lateral pressure of 1.0 GPa for stabilizing the square arrangement. Simulated STM images reveal that, in this case, the underneath water layer and the NaCl contaminant can again be unambiguously distinguished when an h-BN capping layer is used, whereas these features become indistinguish-

able when a graphene capping layer is employed (Extended Data Figure 2). This result further underscores the advantage of using the STM-transparent h-BN capping layer, as discussed above.

#### \* **Probing other phases of 2D ice**

The present setup is also effective for identifying other ordered 2D ice phases. Specifically, when the confinement width between h-BN and Cu(111) is set to 4.8 Å, a nanoconfined “flat rhombic” 2D ice<sup>26</sup> is obtained, where the water arrangement displays zigzag rows and linear columns, under the predicted lateral pressure of 2.6 GPa (Figure 3a, left panel). The corresponding simulated STM image displays pronounced stripe-like features along the rows, with point-like features along the columns (Figure 3a, right panel). While the column features resemble those of the square phase, the row features are quite different. This discrepancy can be attributed to the strengthened hydrogen bonding within the zigzag water chains under higher lateral pressure<sup>29</sup>.

This STM imaging protocol not only captures the stable 2D ice structures, but also enables clear visualization of the key intermediate structures formed during phase transitions, thus providing insights into the phase transformation mechanisms of 2D ice. Previous molecular dynamics simulations employing idealized hydrophobic potentials suggested a broad coexistence region between zigzag (flat rhombic) and square phases<sup>26,27</sup>. Under the h-BN/Cu(111) nanoconfinement, such a coexistence structure is observed at a confinement width of 6.5 Å and a lateral pressure of 3.8 GPa (Figure 3b, left panel), where the square and zigzag arrangements located in the central and edge regions, respectively. The corresponding STM patterns faithfully reflect the coexistence of ordered water phases. Specifically, rectangular units in the center gradually evolve into rhom-

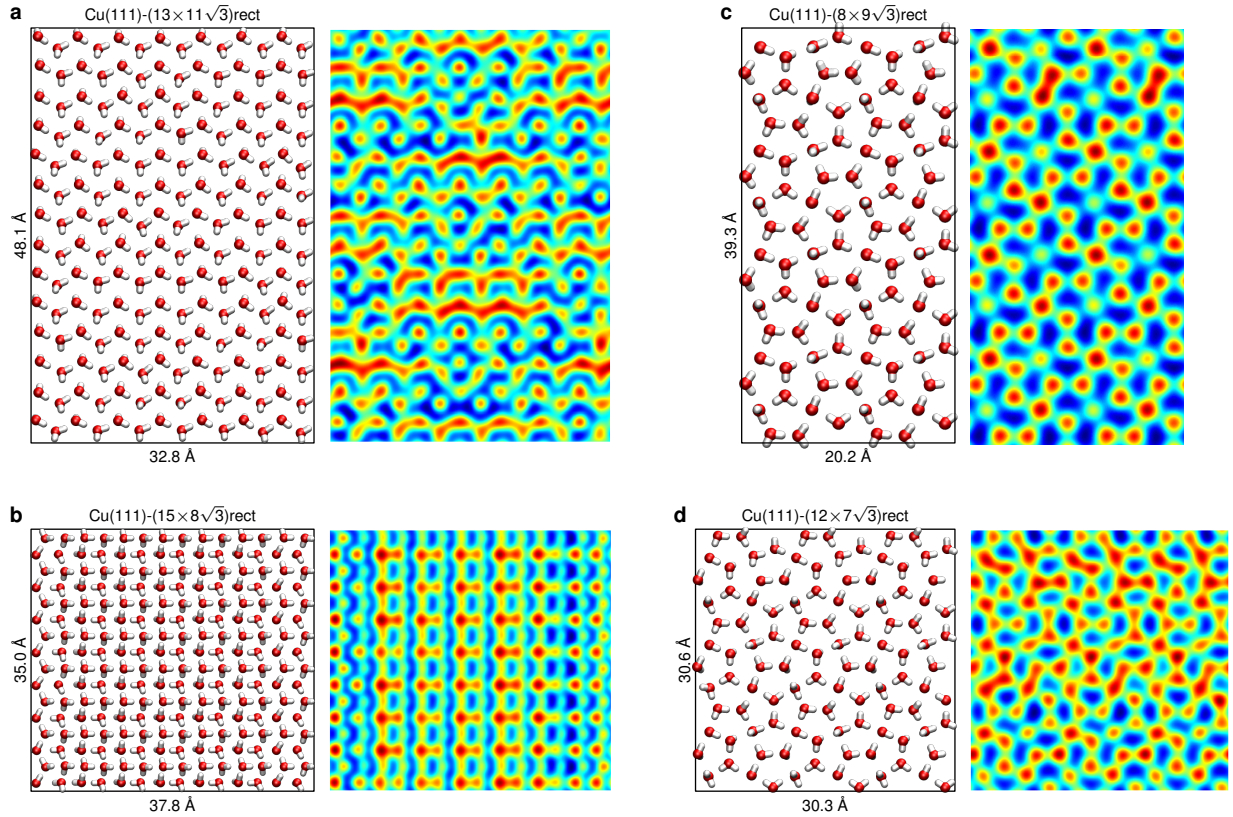


Figure 3: **Probing other 2D ice structures.** Top view of the optimized geometries (left) and the corresponding simulated STM images (right) for the zigzag (a), square/zigzag coexisting (b), pentagonal with rectangle supercell (c), and pentagonal with square supercell (d) 2D ice confined between the h-BN and Cu(111) surface. The lattice constants (in Å) of the heterogeneous layers and the supercell of Cu(111) are labeled. All STM simulations were performed at a bias voltage of  $-0.5$  V.

bic and stripe-like patterns toward the edges (Figure 3b, right panel). Compared to the individual square and zigzag phases, the STM image of the coexisting phase shows alternating rows with periodic bright-dark contrast modulations. This contrast arises from differences in water-substrate interactions across the interface. Specifically, the excessively high surface density induces strong

repulsive interactions between adjacent water rows, leading to buckling and dislocation along the surface normal direction in the 2D ice (Supplementary Figure 2). As a result, the water molecules closer to the metallic substrate dominate the STM contrast, as their enhanced interaction shifts their DOS closer to the Fermi level. This highlights the power of STM imaging in resolving the subtle structural and electronic variations during phase transitions in confined 2D ice.

Under lower lateral pressures, which are typically associated with larger confinement widths, the STM-based detection generally faces greater challenges in identifying the underneath water structures, due to exponentially decaying tunneling currents and reduced structural order. To test the effectiveness of the protocol proposed here, under such demanding conditions, we simulated nanoconfined pentagonal 2D ice at low lateral pressures ranging from 0.1 to 0.2 GPa. Previous theoretical simulations indicated that there are two pentagonal phases, differing in the shape of their unit cells. For the one with a square-like unit cell reported in Ref. 26, the optimal confinement width between h-BN and Cu(111) is determined as 5.6 Å. The corresponding STM image displays a clearly visible pentagonal arrangement of the beneath water molecules, as anticipated (Figure 3c). Notably, this confinement width is slightly smaller than that (5.7 Å) required for the square phase, which is denser. This reflects the influence of the realistic confinement conditions in the practical simulations. When the one with a rectangle-like shaped unit cell from Ref. 25 was adopted, the optimized confinement width increases to the largest value of 6.8 Å. Even under such weak confinement, STM measurements can still effectively penetrate the h-BN layer, enabling unambiguous visualization of the underlying pentagonal structure (Figure 3d). In this case, the contrast variation in the STM image arises again from subtle height differences in the 2D ice

lattice, induced by the realistic water-metal interaction (Supplementary Figure 3).

It is worth reiterating that the key to the success of the current setup in detecting the underneath water arrangements lies in our choice of using h-BN as the capping layer, which has a negligible DOS distribution near the Fermi level (Figure 2 and Extended Data Figure 3). For systems with larger confinement widths, the DOS of h-BN decreases further, which enhances the STM transparency of the capping layer and effectively compensates for the signal attenuation typically associated with increased tip-sample distance. Consequently, chemically resolved images of the underlying water molecules can be obtained for all investigated phases of 2D ice. In contrast, although graphene is widely used to construct confined environments for stabilizing various 2D ice phases, its unique Dirac cone band structure (Supplementary Figure 4) results in a finite and delocalized DOS near the Fermi level. This significantly masks the local electronic signatures of the encapsulated water structures, making it difficult to detect the underneath 2D water structures (Supplementary Figure 5).

For the substrate, a real Cu(111) is used in the current setup, which differs from the idealized confining environments used in previous theoretical studies. Nevertheless, the obtained trend of lateral pressure for various 2D ice phases is in good agreement with prior reports (Figure 4). For instance, using the lattice parameters from Refs. 26 and 27, we find that reducing the interlayer spacing between h-BN and Cu(111) generally leads to higher lateral pressure, and thus denser ice phases (Figure 4 and Supplementary Table 1). The calculated lateral pressures exhibit only minor variations when other 2D material capping layers, such as graphene (Supplementary Table 2),

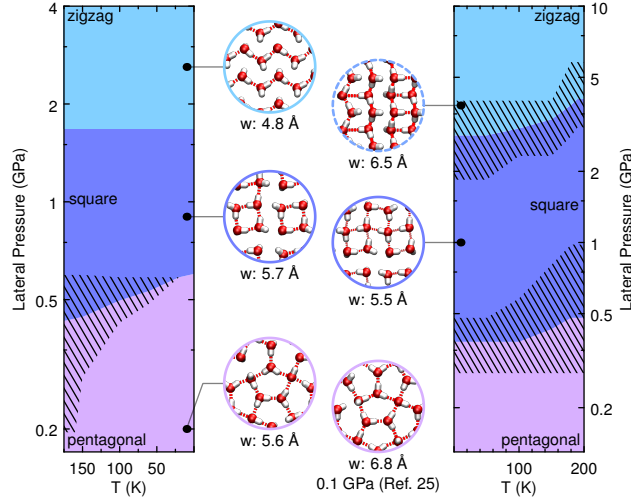


Figure 4: **Correlation between the confinement widths and the lateral pressures.** Summary of the calculated lateral pressures with different confinement widths (labeled values in Å) for the 2D ice confined between a single h-BN capping layer and Cu(111) substrate. These results are generally in good agreement with the previously predicted phase diagrams from Ref. 26 (left) and Ref. 27 (right) with idealized hydrophobic repulsive potentials. The pentagonal phase with a confinement width of 6.8 Å corresponds to the lattice constants in Ref. 25. The dashed areas in the phase diagrams indicate regions of coexistence phases.

are used, which highlights the generality of the simulated pressure-confinement relationship. The most notable exception is the coexistence phase between zigzag and square 2D ice structures. While the predicted lateral pressure (3.6 GPa) for this phase matches the value reported in Ref. 27, the corresponding confinement width is unexpectedly larger than those of lower-density phases. This anomalous behavior suggests that additional external pressurization may be necessary to stabilize this phase under real experimental conditions. It should be stressed that the configurations identified here encompass all known ordered flat 2D ice phases, which also represents the 2D ice

structures over a wide range of temperatures below 170 K (Figure 4). However, the detection of other proposed 2D ice phases, such as the zigzag quasi-bilayer or hexatic ice<sup>26,27</sup>, under extreme conditions (e.g., high temperature or ultrahigh pressure) remains an open challenge. Their observation is hindered by the strong interaction between water and confinement materials, as well as the intrinsic structural disorder, necessitating the development of advanced detection techniques beyond current capabilities.

Finally, we emphasize that the protocol proposed in the present work is fully compatible with current experimental techniques. For example, nanoslits can be pre-fabricated using electron beam lithography, followed by transfer of h-BN flake onto the structure<sup>46</sup>. Water molecules can then be introduced through designed opening windows either at the ends<sup>46</sup> or from the backsides<sup>11</sup>. Subnanometer-confined water molecules can be achieved<sup>11</sup>, provided that sagging of the h-BN capping layer during water infiltration can be prevented<sup>46</sup>. Alternatively, a recently developed approach involves first adsorbing water molecules onto a substrate under controlled humidity and temperature, followed by direct transfer of an h-BN flake to encapsulate the layer<sup>47</sup>. This method has successfully produced subnanometer-confined water molecules between diamond and h-BN, offering precise control over confinement thickness<sup>47</sup>. Notably, a closely analogous nanoslit, featuring a CO monolayer intercalated between Pt(111) and h-BN, has already been realized using a protocol similar to the first approach<sup>33</sup>. This experimental demonstration strongly supports the feasibility of the present design: a molecular layer confined between a metallic surface and a h-BN capping layer, as proposed in the current work.

## **Conclusion**

In summary, this work proposes a unique protocol, using STM to investigate the phases of the ordered 2D ice. In contrast to the idealized hydrophobic potentials used in previous studies, it consists of a wide bandgap h-BN as the capping layer and the Cu(111) surface as the substrate. First-principles theoretical calculations reveal that STM measurements can penetrate the h-BN layer, enabling chemically resolved characterization of the underneath water structures, a capability inaccessible to other experimental techniques. Consequently, the STM images faithfully reflect the molecular arrangement of “square” ice previously inferred from TEM studies, while clearly distinguishing it from the potential NaCl contaminant, resolving a long-standing debate in the field of 2D ice. Moreover, this protocol allows unambiguous identification of all other previously predicted ordered 2D ice phases, including the coexisting phase under various lateral pressures. This makes STM a practical and powerful tool for probing 2D ice phases over a wide range of lateral pressures. These findings not only deepen our understanding of the microscopic structure of monolayer water but also offer valuable insights into interactions between water and metal surfaces in confined environments, lifting the curtain on the study of phases of 2D ice at the atomic scale..

## **Methods**

### **Model construction**

The slab model was employed to simulate the 2D heterogeneous structures, where the metallic substrate was mimicked by a three-layer Cu(111) slab. To avoid artificial deformation, the 2D

ice and Cu(111) unit cells were expanded such that the lattice mismatch ratio between the two supercells is less than 1%. A vacuum region exceeding 15 Å was added above the capping layer to render the inter-slab interactions along the  $z$ -direction negligible.

### **Structure optimization and lateral pressure evaluation**

The initial structures were optimized using the PBE functional<sup>48</sup>, augmented with the D3 version of Grimme’s dispersion correction with Becke-Johnson damping<sup>49,50</sup>, as implemented in the CP2K package<sup>51</sup>. The Goedecker, Teter, and Hutter (GTH) pseudopotentials<sup>52</sup> and the associated optimized Gaussian basis sets for molecular calculations<sup>53</sup> were used. Specifically, the triple zeta basis sets (TZVP-MOLOPT-GTH) were used for describing valence electrons in oxygen and hydrogen, while the double zeta basis sets (DZVP-MOLOPT-SR-GTH) were used for copper, boron, nitrogen, and carbon, providing a good balance between accuracy and computational efficiency. In the Gaussian and Plane Waves (GPW) method, the plane wave cutoff for the finest grid level and the mapping reference grid were set to 480 and 60 Rydberg, respectively. Periodic boundary conditions were applied in all three dimensions. For  $k$ -point sampling, the  $\Gamma$ -only method was used during geometrical optimizations, justified by the large supercell sizes (the lengths of the supercells are all greater than 20 Å), which minimize finite-size effects. The conjugate gradient algorithm with four steps was employed to accelerate the optimizations. Specifically, 1) Relaxation of the  $z$ -coordinates of the 2D ice and the topmost two Cu(111) slab layers; 2) Full relaxation of all degrees of the freedom of the 2D ice; 3) Optimization of the  $xy$ -coordinates of the capping layer and the topmost two Cu(111) slab layers; 4) Simultaneous optimization of all degree of the freedoms of the 2D ice and the topmost two Cu(111) slab layers as well as the  $xy$ -coordinates of

the capping layer. During these steps, the positions of the bottom Cu(111) slab layer and the  $z$ -coordinates of the capping layer were fixed to mimic the metallic bulk and to simulate experimental conditions for confinement. Based on the optimized geometries, the stress tensors were calculated for systems with and without the presence of the 2D ice monolayer. The true stress tensor of the 2D ice monolayer was obtained by subtracting the latter from the former. Then, as suggested by the previous works,<sup>25,54</sup> the lateral pressure exerted on the 2D ice was evaluated as

$$P = \frac{L_z}{2h} (\sigma_{xx} + \sigma_{yy}), \quad (1)$$

where  $\sigma_{xx}$  and  $\sigma_{yy}$  are the diagonal elements of the stress tensor of the ice layer,  $L_z$  is the length of the supercell in the  $z$ -direction and  $h$  is the confinement width (i.e., the distance between the h-BN capping layer and the Cu(111) substrate).

### Electronic structure calculation

On top of the optimized geometrical structures, the DOS and partial charge analyses were conducted using the Vienna Ab-initio Simulation Package (VASP)<sup>55</sup>. Calculations employed either the PBE<sup>48</sup> or xPBE<sup>56</sup> functionals via Libxc<sup>57</sup>. Projector augmented-wave (PAW) pseudopotentials<sup>58</sup> were used to describe core electrons, while plane-wave basis sets with a kinetic energy cutoff of 400 eV were used to describe valence electrons. For Brillouin zone integration, a dense  $k$ -point mesh was adopted, ensuring a maximum spacing of less than  $0.038 \text{ \AA}^{-1}$ , in combination with the tetrahedron method and Blöchl corrections to achieve high accuracy of electronic structures. A dipole correction was applied along the  $z$ -direction to mitigate artificial electrostatic interactions between periodically repeated images.

## **STM simulation**

Based on the obtained electronic structures, all STM images were simulated using the Tersoff-Hamann theory<sup>31,35-37</sup>, assuming for conventional metallic tips under a sample bias of  $-0.5$  V in constant-current mode. To account for finite mapping resolution, all calculated STM images were filtered by a Gaussian smearing with a bandwidth of  $0.75$  Å. The isovalue settings for different systems were summarized in Supplementary Table 3. The STM images obtained using the PBE and xPBE functionals exhibit no observable differences, demonstrating the robustness of the images.

## **Acknowledgements**

This work was supported by the National Key R&D Program of China (2024YFA1208104), the National Natural Science Foundation of China (Nos. 22393911 and 22473028), the Innovation Program for Quantum Science and Technology (Nos. 2021ZD0303301 and 2021ZD0303305), and the robotic AI-Scientist platform of Chinese Academy of Science.

## **Author contributions**

S.D. and X.X. conceived and supervised the project. B.W. and J.W. performed the calculations. S.D., X.X. and B.W. analyzed the data and wrote the manuscript. All authors reviewed, edited, and approved the final manuscript.

## Competing interests

The authors declare no competing interests.

## Additional information

**Supplementary Information** Supplementary information is available in the online version of the paper.

Reprints and permissions information is available online at [www.nature.com/reprints](http://www.nature.com/reprints).

**Correspondence** Correspondence and requests for materials should be addressed to Sai Duan and Xin Xu.

**Corresponding Authors** Sai Duan (email: [duansai@fudan.edu.cn](mailto:duansai@fudan.edu.cn)) and Xin Xu (email: [xxchem@fudan.edu.cn](mailto:xxchem@fudan.edu.cn))

## References

1. Szent-Györgyi, A. Biology and pathology of water. *Perspect. Biol. Med.* **14**, 239–249 (1971).
2. Ball, P. Water is an active matrix of life for cell and molecular biology. *Proc. Natl. Acad. Sci. U.S.A.* **114**, 13327–13335 (2017).
3. Ball, P. Water - an enduring mystery. *Nature* **452**, 291–292 (2008).
4. Pettersson, L. G. M., Henchman, R. H. & Nilsson, A. Water-the most anomalous liquid. *Chem. Rev.* **116**, 7459–7462 (2016).

5. Eisenberg, D. & Kauzmann, W. *The Structure and Properties of Water* (Oxford University Press, 2005).
6. Brini, E. *et al.* How water's properties are encoded in its molecular structure and energies. *Chem. Rev.* **117**, 12385–12414 (2017).
7. Tammann, G. Ueber die grenzen des festen zustandes IV. *Ann. Phys.* **307**, 1–31 (1900).
8. Hansen, T. C. The everlasting hunt for new ice phases. *Nat. Commun.* **12**, 3161 (2021).
9. Rosu-Finsen, A. *et al.* Medium-density amorphous ice. *Science* **379**, 474–478 (2023).
10. Gopinadhan, K. *et al.* Complete steric exclusion of ions and proton transport through confined monolayer water. *Science* **363**, 145–148 (2019).
11. Fumagalli, L. *et al.* Anomalously low dielectric constant of confined water. *Science* **360**, 1339–1342 (2018).
12. Nair, R. R., Wu, H. A., Jayaram, P. N., Grigorieva, I. V. & Geim, A. K. Unimpeded permeation of water through helium-leak-tight graphene-based membranes. *Science* **335**, 442–444 (2012).
13. Neek-Amal, M., Peeters, F. M., Grigorieva, I. V. & Geim, A. K. Commensurability effects in viscosity of nanoconfined water. *ACS Nano* **10**, 3685–3692 (2016).
14. Guo, W.-Q., Deng, J.-W. & Wang, B.-B. Molecular dynamics simulations on heat transport of nanoconfined water under electric fields: Effect of nanochannel size. *J. Phys. Chem. B* **129**, 348–359 (2025).

15. Israelachvili, J. & Wennerström, H. Role of hydration and water structure in biological and colloidal interactions. *Nature* **379**, 219–225 (1996).
16. Kavokine, N., Bocquet, M.-L. & Bocquet, L. Fluctuation-induced quantum friction in nanoscale water flows. *Nature* **602**, 84–90 (2022).
17. Nie, S., Feibelman, P. J., Bartelt, N. C. & Thürmer, K. Pentagons and heptagons in the first water layer on Pt(111). *Phys. Rev. Lett.* **105**, 026102 (2010).
18. Ma, R. *et al.* Atomic imaging of the edge structure and growth of a two-dimensional hexagonal ice. *Nature* **577**, 60–63 (2020).
19. Yang, D.-S. & Zewail, A. H. Ordered water structure at hydrophobic graphite interfaces observed by 4D, ultrafast electron crystallography. *Proc. Natl. Acad. Sci. U.S.A.* **106**, 4122–4126 (2009).
20. Kimmel, G. A. *et al.* No confinement needed: Observation of a metastable hydrophobic wetting two-layer ice on graphene. *J. Am. Chem. Soc.* **131**, 12838–12844 (2009).
21. Xu, K., Cao, P. & Heath, J. R. Graphene visualizes the first water adlayers on mica at ambient conditions. *Science* **329**, 1188–1191 (2010).
22. He, K. T., Wood, J. D., Doidge, G. P., Pop, E. & Lyding, J. W. Scanning tunneling microscopy study and nanomanipulation of graphene-coated water on mica. *Nano Lett.* **12**, 2665–2672 (2012).

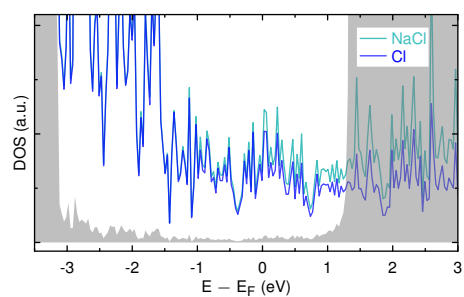
23. Li, Q., Song, J., Besenbacher, F. & Dong, M. Two-dimensional material confined water. *Acc. Chem. Res.* **48**, 119–127 (2015).
24. Algara-Siller, G. *et al.* Square ice in graphene nanocapillaries. *Nature* **519**, 443–445 (2015).
25. Chen, J., Schusteritsch, G., Pickard, C. J., Salzmann, C. G. & Michaelides, A. Two dimensional ice from first principles: Structures and phase transitions. *Phys. Rev. Lett.* **116**, 025501 (2016).
26. Kapil, V. *et al.* The first-principles phase diagram of monolayer nanoconfined water. *Nature* **609**, 512–516 (2022).
27. Lin, B., Jiang, J., Zeng, X. C. & Li, L. Temperature-pressure phase diagram of confined monolayer water/ice at first-principles accuracy with a machine-learning force field. *Nat. Commun.* **14**, 4110 (2023).
28. Jiang, J. *et al.* Rich proton dynamics and phase behaviours of nanoconfined ices. *Nat. Phys.* **20**, 456–464 (2024).
29. Ravindra, P., Advincula, X. R., Schran, C., Michaelides, A. & Kapil, V. Quasi-one-dimensional hydrogen bonding in nanoconfined ice. *Nat. Commun.* **15**, 7301 (2024).
30. Zhou, W. *et al.* The observation of square ice in graphene questioned. *Nature* **528**, E1–E2 (2015).
31. Duan, S., Zhang, I. Y., Xie, Z. & Xu, X. Identification of water hexamer on Cu(111) surfaces. *J. Am. Chem. Soc.* **142**, 6902–6906 (2020).

32. Wickramaratne, D., Weston, L. & Van de Walle, C. G. Monolayer to bulk properties of hexagonal boron nitride. *J. Phys. Chem. C* **122**, 25524–25529 (2018).
33. Wu, H. *et al.* Dynamic nanoscale imaging of enriched CO adlayer on Pt(111) confined under h-BN monolayer in ambient pressure atmospheres. *Nano Res.* **12**, 85–90 (2019).
34. Kirchhoff, A., Deilmann, T., Krüger, P. & Rohlfing, M. Electronic and optical properties of a hexagonal boron nitride monolayer in its pristine form and with point defects from first principles. *Phys. Rev. B* **106**, 045118 (2022).
35. Tersoff, J. & Hamann, D. R. Theory of the scanning tunneling microscope. *Phys. Rev. B* **31**, 805–813 (1985).
36. Duan, S., Tian, G. & Xu, X. A general framework of scanning tunneling microscopy based on Bardeen's approximation for isolated molecules. *JACS Au* **3**, 86–92 (2023).
37. Duan, S. & Xu, X. Accurate simulations of scanning tunneling microscope: Both tip and substrate states matter. *J. Phys. Chem. Lett.* **14**, 6726–6735 (2023).
38. Zhu, Y. *et al.* Reconstructing pristine molecular orbitals from scanning tunneling microscope images via artificial intelligence approaches. *JACS Au* **5**, 3163–3170 (2025).
39. Geim, A. K. & Novoselov, K. S. The rise of graphene. *Nat. Mater.* **6**, 183–191 (2007).
40. Abergel, D., Apalkov, V., Berashevich, J., Ziegler, K. & Chakraborty, T. Properties of graphene: a theoretical perspective. *Adv. Phys.* **59**, 261–482 (2010).

41. Gross, L., Mohn, F., Moll, N., Liljeroth, P. & Meyer, G. The chemical structure of a molecule resolved by atomic force microscopy. *Science* **325**, 1110–1114 (2009).
42. Duan, S. *et al.* Theoretical modeling of plasmon-enhanced Raman images of a single molecule with subnanometer resolution. *J. Am. Chem. Soc.* **137**, 9515–9518 (2015).
43. Duan, S., Tian, G. & Luo, Y. Visualization of vibrational modes in real space by tip-enhanced non-resonant Raman spectroscopy. *Angew. Chem. Int. Ed.* **55**, 1041–1045 (2016).
44. Duan, S., Rinkevicius, Z., Tian, G. & Luo, Y. Optomagnetic effect induced by magnetized nanocavity plasmon. *J. Am. Chem. Soc.* **141**, 13795–13798 (2019).
45. Qiu, F. *et al.* Optical images of molecular vibronic couplings from tip-enhanced fluorescence excitation spectroscopy. *JACS Au* **2**, 150–158 (2022).
46. Pagliero, D. *et al.* Slow water in engineered nanochannels revealed by color-center-enabled sensing. *Nano Lett.* **25**, 9960–9966 (2025).
47. Zheng, W. *et al.* Observation of liquid-solid transition of nanoconfined water at ambient temperature (2024). ArXiv:2412.15001.
48. Perdew, J. P., Burke, K. & Ernzerhof, M. Generalized gradient approximation made simple. *Phys. Rev. Lett.* **77**, 3865–3868 (1996).
49. Grimme, S., Antony, J., Ehrlich, S. & Krieg, H. A consistent and accurate ab initio parametrization of density functional dispersion correction (DFT-D) for the 94 elements H–Pu. *J. Chem. Phys.* **132**, 154104 (2010).

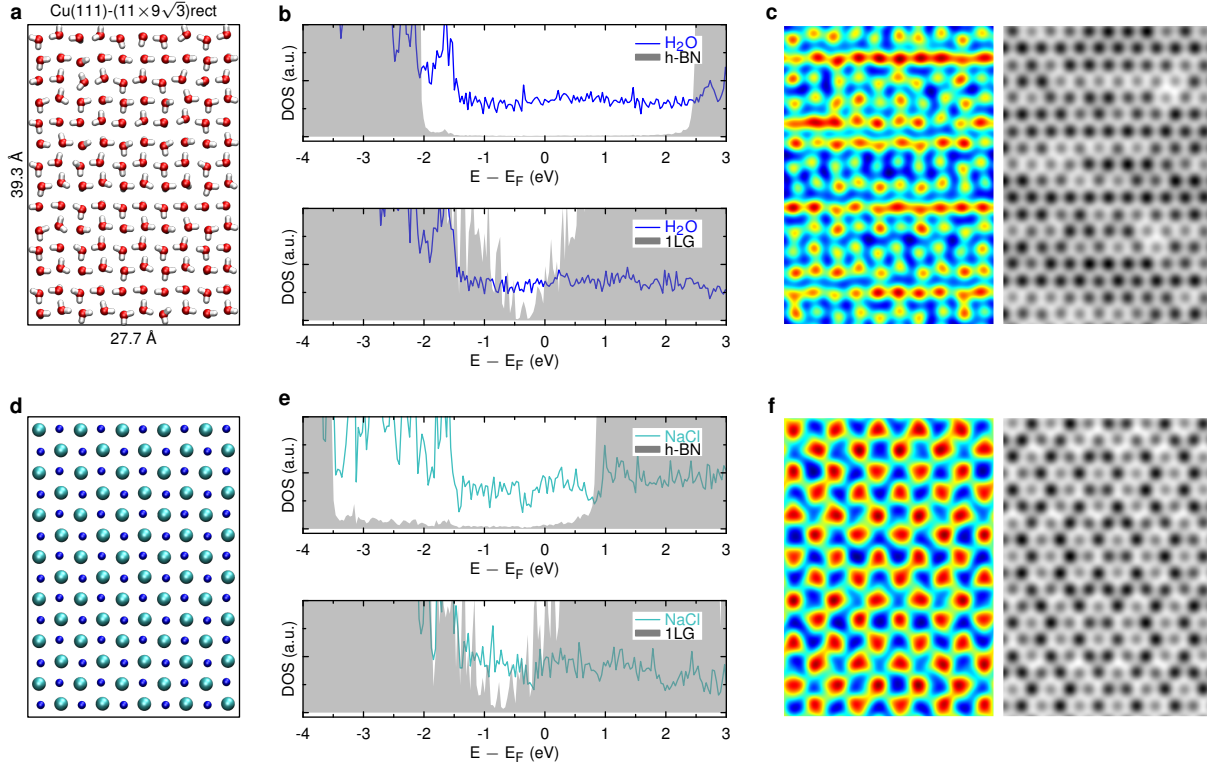
50. Grimme, S., Ehrlich, S. & Goerigk, L. Effect of the damping function in dispersion corrected density functional theory. *J. Comput. Chem.* **32**, 1456–1465 (2011).
51. Kühne, T. D. *et al.* CP2K: An electronic structure and molecular dynamics software package - quickstep: Efficient and accurate electronic structure calculations. *J. Chem. Phys.* **152**, 194103 (2020).
52. Goedecker, S., Teter, M. & Hutter, J. Separable dual-space gaussian pseudopotentials. *Phys. Rev. B* **54**, 1703–1710 (1996).
53. VandeVondele, J. & Hutter, J. Gaussian basis sets for accurate calculations on molecular systems in gas and condensed phases. *J. Chem. Phys.* **127**, 114105 (2007).
54. Corsetti, F., Matthews, P. & Artacho, E. Structural and configurational properties of nanoconfined monolayer ice from first principles. *Sci. Rep.* **6**, 18651 (2016).
55. Kresse, G. & Furthmüller, J. Efficient iterative schemes for ab initio total-energy calculations using a plane-wave basis set. *Phys. Rev. B* **54**, 11169–11186 (1996).
56. Xu, X. & Goddard III, W. A. The extended Perdew-Burke-Ernzerhof functional with improved accuracy for thermodynamic and electronic properties of molecular systems. *J. Chem. Phys.* **121**, 4068–4082 (2004).
57. Lehtola, S., Steigemann, C., Oliveira, M. J. T. & Marques, M. A. L. Recent developments in libxc — a comprehensive library of functionals for density functional theory. *SoftwareX* **7**, 1–5 (2018).

58. Kresse, G. & Joubert, D. From ultrasoft pseudopotentials to the projector augmented-wave method. *Phys. Rev. B* **59**, 1758–1775 (1999).

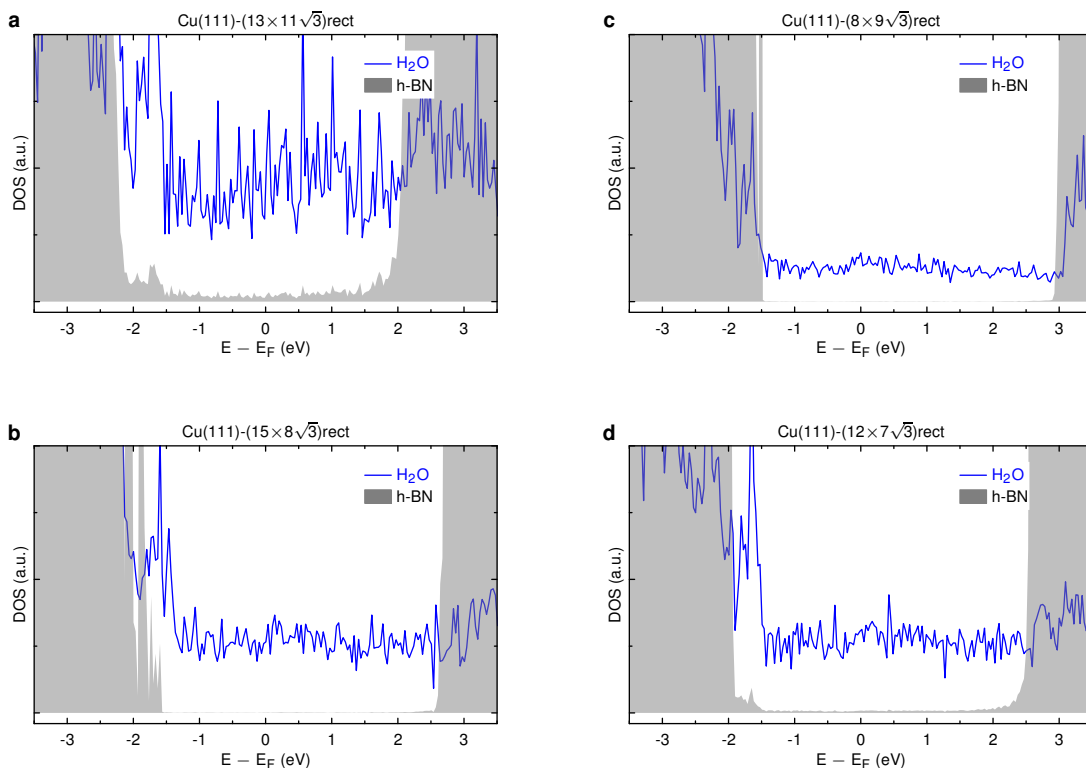


Extended Data Figure 1: **Detailed Projected DOS for the NaCl monolayer capped by h-BN.**

The cyan and blue lines represent the projected DOS contributed from the total NaCl layer and that from the Cl atoms, respectively. The projected DOS of the h-BN (gray region) capping layer is also depicted for comparison.



Extended Data Figure 2: **Identification of an alternative square 2D ice.** **a**, Top view of the optimized geometry of the square 2D ice that has the primitive water unit cell reported in Ref. 25, confined between a single h-BN layer and Cu(111) surface with a confinement width of 5.5 Å. The lattice constants (in Å) of the heterogeneous layers and the supercell of Cu(111) are labeled. **b**, Projected density of state (DOS) for the alternative square 2D ice systems with a single h-BN layer (top) and a single graphene layer (1LG, bottom) as the capping layer. **c**, Simulated STM images for confined square 2D ice with h-BN (left) and graphene (right) as the capping layer. **d**, Top view after replacing water with NaCl in panel (a). **e**, Projected DOS for the NaCl systems capped by h-BN (top) and graphene layer (1LG, bottom) capping NaCl. **f**, Simulated STM images of confined NaCl with a single h-BN layer (left) and a single graphene layer (right) as the capping layer. All STM simulations were performed at a sample bias of  $-0.5$  V.



Extended Data Figure 3: **Projected DOS for other 2D ice structures.** Calculated projected DOS of the zigzag (a), square/zigzag coexisting (b), pentagonal with rectangle supercell (c), and pentagonal with square supercell (d) 2D ice confined between the h-BN and Cu(111) surface. The blue line and gray region represent the projected DOS contributed from the 2D ice layer and that from the h-BN capping layer, respectively. The supercells of Cu(111) are also indicated.